A state-insensitive, compensated nanofiber trap

A state-insensitive, compensated nanofiber trap

C Lacroûte[1,4]**, K S Choi**[1,2,4]**, A Goban**[1,4]**, D J Alton**[1]**, D Ding**[1]**,
N P Stern**[1,5] **and H J Kimble**[1,3]

[1] Norman Bridge Laboratory of Physics, 12-33, California Institute of
Technology, Pasadena, CA 91125, USA
[2] Spin Device Research Center, Korea Institute of Science and Technology,
39-1 Hawolgok-dong, Seongbuk-gu, Seoul 136-791, Korea
E-mail: hjkimble@its.caltech.edu

Abstract. Laser trapping and interfacing of laser-cooled atoms in an optical
fiber network is an important tool for quantum information science. Following
the pioneering work of Balykin *et al* (2004 *Phys. Rev.* A **70** 011401) and
Vetsch *et al* (2010 *Phys. Rev. Lett.* **104** 203603), we propose a robust method
for trapping single cesium atoms with a two-color state-insensitive evanescent
wave around a dielectric nanofiber. Specifically, we show that vector light shifts
(i.e. effective inhomogeneous Zeeman broadening of the ground states) induced
by the inherent ellipticity of the forward-propagating evanescent wave can be
effectively canceled by a backward-propagating evanescent wave. Furthermore,
by operating the trapping lasers at the magic wavelengths, we remove the
differential scalar light shift between ground and excited states, thereby allowing
for resonant driving of the optical D_2 transition. This scheme provides a
promising approach to trap and probe neutral atoms with long trap and coherence
lifetimes with realistic experimental parameters.

[3] Author to whom any correspondence should be addressed.

[4] These authors contributed equally to this work.

[5] Current address: Department of Physics and Astronomy, Northwestern University, 2145 Sheridan Road, Evanston,
IL 60208, USA.

IOP Institute of Physics Φ DEUTSCHE PHYSIKALISCHE GESELLSCHAFT

Contents

1. Introduction

The development of a matter–light quantum interface using cold atoms and optical fibers has been an active field of research over the last few years [1]. Recent advances toward this goal include the observation of electromagnetically induced transparency and the loading of ultracold atoms in hollow-core optical fibers [2–5], as well as the trapping and probing of atomic ensembles via the evanescent fields surrounding tapered nanofibers [6–9]. While prominent examples of off-resonant interaction between evanescent waves and matter have used a plane dielectric geometry for atom optics and interferometry [10, 11] as well as for surface traps of quantum degenerate gases [12–14], recent progress in atom–light interactions with optical waveguides [4, 5, 7–9] set the stage for the fiber integration of free-space quantum systems in a quantum network via quantum-state transfer between matter and light [15–18] and for strong coupling of single atoms and photons trapped near microcavities [19–24]. Furthermore, these effective one-dimensional (1D) systems may be applied to investigating quantum many-body phenomena in low dimensions with long-range interactions mediated by the waveguide [25–28].

One major drawback of many optical traps is that spatially inhomogeneous energy shifts $U(\mathbf{r})$ generally depend on the atomic electronic state, limiting the long-lived trap and coherence times necessary for repeated coherent operations [29]. This is traditionally alleviated by constructing a *state-insensitive* optical trap designed to decouple atomic transition frequencies from the spatially varying potential of each electronic state [30]. Specifically, in the 'magic' wavelength conditions, the differential response of the dynamic scalar polarizabilities $\alpha^{(0)}(\omega)$ for the ground and excited states $\alpha^{(0)}_{|g\rangle}, \alpha^{(0)}_{|e\rangle}$ at the optical frequency ω can be tailored such that both levels are perturbed identically with $\alpha^{(0)}_{|g\rangle} = \alpha^{(0)}_{|e\rangle}$. This leads to a vanishing differential atomic level shift $\delta U_{\text{scalar}} = 0$ [30–34]. Differential shifts for the hyperfine ground states can be minimized by using far off-resonant beams, whereas Zeeman coherence can be conveniently protected by using linearly polarized light in which the vector light shifts are zero.

Although such magic wavelengths can be used for nanofiber traps [35], the strongly guiding nature of the waveguide inevitably leads to non-negligible longitudinal electric fields $\mathbf{E}_z$ in the evanescent region, which are out of phase with the transverse field $\mathbf{E}_\perp = (\mathbf{E}_x, \mathbf{E}_y)$. Here, z refers to the direction parallel to the fiber axis, while x and y are the coordinates perpendicular to the fiber axis. The resulting local polarization at location $\mathbf{r}$ is in general elliptical even for linearly polarized input beams, and induces vector shifts U_{vector}. The differential vector shift δU_{vector} in turn manifests itself as a 'fictitious magnetic field', leading to inhomogeneous Zeeman broadening [36]. Furthermore, the spatially varying elliptical polarization of the evanescent field on a scale $\delta r < \lambda$ renders it difficult to cancel δU_{vector} using bias fields, resulting in increased heating rate [29] and limited coherence time [37].

Building upon the recent realization of a nanofiber trap as proposed in [38] and demonstrated in [6, 39], we propose a promising strategy for a state-insensitive evanescent field trap. Differential scalar shifts δU_{scalar} between $|g\rangle$ and $|e\rangle$ are canceled using 'magic' wavelength conditions. The inhomogeneous Zeeman broadening δU_{vector} caused by a forward propagating blue-detuned field $\mathbf{E}^{(\text{fwd})}$ is canceled by a backward propagating field $\mathbf{E}^{(\text{bwd})}$ with a small relative frequency detuning δ_{fb}. Thus, our scheme can compensate for the light shifts of the strongly guided evanescent waves to the first order in the space external to the dielectric fiber, leading to favorable parameters for the realization of a long-lived fiber-integrated quantum memory and resonant coupling to ultra-high-quality micro-cavities based on optically trapped atoms.

The paper is organized as follows. Section 2 presents our scheme for generating a state-insensitive nanofiber trap. We start by introducing the general Hamiltonian for the atom–light dipole interaction (section 2.1); we next discuss the principle of evanescent optical traps around a nanofiber (section 2.2), before describing in more detail the spatially varying electric field polarization of the evanescent wave (section 2.3). We finally show how to cancel the subsequent vector (section 2.4) and scalar (section 2.5) light shifts induced on the D_2 transition of cesium. In section 3, the benefits of using our proposed scheme are shown. We first describe the total Hamiltonian used for calculating the trapping potentials (section 3.1). We then plot the adiabatic potentials obtained for the ground ($6S_{1/2}$) and excited ($6P_{3/2}$) states of Cs using the parameters in [6] and illustrate the effects of the vector shifts (section 3.2). Finally, the potentials obtained with our scheme are shown and an estimate of residual differential shifts is provided (section 3.2). We then proceed to our concluding remarks in section 4.

2. A state-insensitive nanofiber trap

In this section, we discuss an *ab initio* calculation of the optical nanofiber trap for atomic cesium. We show that the light shifts caused by the elliptically polarized components of the fiber's evanescent field are not negligible. We then propose a scheme to cancel these shifts and generate a two-color, state-insensitive, 3D trap for Cs atoms along the nanofiber.

2.1. ac Stark shift Hamiltonian

We start by considering the Hamiltonian for an atom interacting with an electric field $\mathbf{E}$ in the dipole approximation:

$$\hat{H}_{\text{ls}} = -\hat{\mathbf{d}} \cdot \hat{\mathbf{E}}, \tag{1}$$

where $\hat{\mathbf{d}}$ is the electric dipole operator and $\hat{\mathbf{E}}$ is the electric field operator. Taking into account the atomic hyperfine structure, this Hamiltonian can be decomposed into its spherical tensor components parameterized by the dynamic polarizability $\alpha(\omega)$ [40–42]:

$$
\begin{aligned}
\hat{H}_{\mathrm{ls}} &= \hat{H}_0 + \hat{H}_1 + \hat{H}_2 \\
&= \alpha^{(0)} \hat{\mathbf{E}}^{(-)} \cdot \hat{\mathbf{E}}^{(+)} + \mathrm{i}\alpha^{(1)} \frac{(\hat{\mathbf{E}}^{(-)} \times \hat{\mathbf{E}}^{(+)}) \cdot \hat{\mathbf{F}}}{F} \\
&\quad + \sum_{\mu,\nu} \alpha^{(2)} \hat{E}_\mu^{(-)} \hat{E}_\nu^{(+)} \frac{3}{F(2F-1)} \left[\frac{1}{2}(\hat{F}_\mu \hat{F}_\nu + \hat{F}_\nu \hat{F}_\mu) - \frac{1}{3}\hat{F}^2 \delta_{\mu\nu} \right],
\end{aligned} \tag{2}
$$

where $\alpha^{(0)}$, $\alpha^{(1)}$ and $\alpha^{(2)}$ are the scalar, vector and tensor atomic dynamic polarizabilities, $\hat{\mathbf{E}}^{(+)}$ and $\hat{\mathbf{E}}^{(-)}$ are the positive and negative frequency components of the electric field, $\hat{\mathbf{F}} = \hat{\mathbf{I}} + \hat{\mathbf{J}}$ is the atomic total angular momentum operator, with $\hat{\mathbf{I}}$ and $\hat{\mathbf{J}}$ the nuclear and electronic angular momentum operators, $\mu, \nu \in \{-1, 0, 1\}$ are components in the spherical tensor basis, and $\hat{H}_0$, $\hat{H}_1$ and $\hat{H}_2$ are the terms associated with the scalar, vector and tensor light shifts, respectively. The light shifts U_{scalar}, U_{vector} and U_{tensor} arising from each term have been expressed explicitly in [40, 41].

For two-level atoms with ground and excited states $|g\rangle$, $|e\rangle$, the scalar shift U_{scalar} can be approximated by $U_{\mathrm{scalar}} \propto |\mathbf{E}|^2/\delta$ for detunings $\delta = \omega - \omega_a$ large compared to the excited state decay rate Γ, where ω is the electric field angular frequency and ω_{a} is the $|g\rangle \to |e\rangle$ transition frequency. The ground state will experience a repulsive potential for blue-detuned ($\delta > 0$) electric fields, and an attractive potential for red-detuned ($\delta < 0$) electric fields. The scalar dynamic polarizability $\alpha^{(0)}$ is in general different for the states $|g\rangle$ and $|e\rangle$, resulting in a differential scalar shift and a mismatch of the ground and excited state potentials. For the typically anti-trapped excited state, near-resonant driving of the transition by an additional beam with frequency $\omega_2 \simeq \omega_{\mathrm{a}}$ can cause significant heating of a trapped atom [29]. This situation can be remedied by the use of 'magic' wavelengths for which $\alpha^{(0)}_{|g\rangle} = \alpha^{(0)}_{|e\rangle}$ [30–32, 34].

The vector term $\hat{H}_1$ of equation (2) induces a Zeeman-like splitting proportional to a projection of the total atomic angular momentum $\mathbf{F}$ and arises from a so-called 'fictitious magnetic field' proportional to the ellipticity of the electric field [36]. In the case of a free-space plane wave propagating along the z-axis, $\hat{H}_1$ can be expressed in terms of the Stokes operators $\hat{\mathbf{S}} = (\hat{S}_0, \hat{S}_x, \hat{S}_y, \hat{S}_z)$ as [41]

$$
\hat{H}_1 \propto \alpha^{(1)}(\omega)\epsilon \frac{\hat{F}_z}{F}, \tag{3}
$$

where $\epsilon = \langle \hat{S}_z \rangle / \langle \hat{S}_0 \rangle = \frac{|E_{+1}|^2 - |E_{-1}|^2}{|E_{+1}|^2 + |E_{-1}|^2}$ is the ellipticity of the electric field. For an elliptically polarized beam, the vector shift can be as large as the scalar shift, and can, for example, be used to cancel the differential light shifts of rubidium atoms confined in a 3D optical lattice [43].

The last term $\hat{H}_2$ in equation (2) represents the tensor shift. It vanishes for atoms with total angular momentum $F = 1/2$ [41]. In the case of the D_2 transition of Cs, which we consider here, it will depend only on the electronic angular momentum $\hat{\mathbf{J}}$ for detunings large compared to the $6\mathrm{P}_{3/2}$ excited state hyperfine structure, and vanish for $J = \frac{1}{2}$ [40, 41]. It will therefore only act on the excited state of the Cs D_2 transition, inducing shifts on the Zeeman $m_{F'}$ sublevels proportional to $m_{F'}^2$.
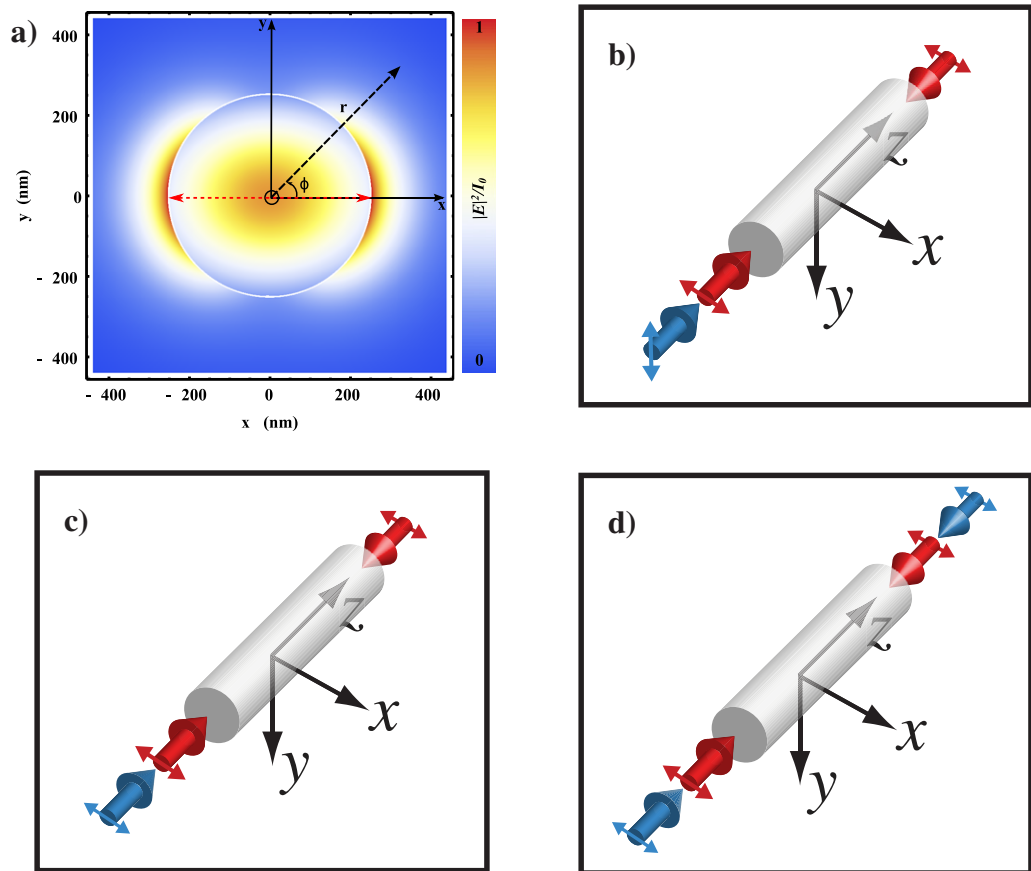
Figure 1. Trapping schemes. (a) Field intensity $|E|^2$ in the plane transverse to the fiber for a single, x-polarized beam at $\lambda = 937$ nm. $|E|^2$ is normalized to the intensity just outside the fiber $I_0 = |E(r = a_+, \phi = 0)|^2$, with $a = 250$ nm and $a_+ = a + |r - a|, r \rightarrow a$. The red dashed arrow indicates the input polarization. (b) Trapping scheme used in [6]. Red (blue)-detuned beams are shown by red (blue) thick arrows. Input polarizations are shown by the thin arrows. A single, y-polarized blue-detuned beam is used. (c) Three-beam scheme with parallel x-polarizations. All beams have an intensity maximum in the $x-y$ plane along the direction of the input polarization. (d) A second x-polarized blue-detuned beam is added to compensate for the vector shifts, as discussed in the main text.

2.2. Evanescent optical traps using the fundamental mode of the waveguide

When the radius a of an optical fiber is reduced well below the propagating field wavelength λ, the resulting cladding-to-air waveguide supports only the 'hybrid' fundamental mode HE_{11} [7, 44]. In this strongly guiding regime, a significant fraction of energy of the HE_{11} mode is carried in the form of an evanescent wave outside of the nanofiber. The evanescent field intensity is azimuthally asymmetric when the input polarization is linear [7, 44]. Figure 1(a) shows the electric field intensity $|E|^2 = |E_x|^2 + |E_y|^2 + |E_z|^2$ in a plane transverse to the fiber for a single,

linearly polarized beam. The unit vectors $(\mathbf{e}_x, \mathbf{e}_y, \mathbf{e}_z)$ form the basis of the (x, y, z) frame, and (r, ϕ) are the cylindrical coordinates in the transverse plane (x, y).

By appropriately combining blue-detuned and red-detuned fields $\mathbf{E}_{\text{red}}$ and $\mathbf{E}_{\text{blue}}$ in an optical nanofiber, an atomic trapping potential can be engineered from the evanescent electric fields [38]. Different configurations can be used for obtaining 3D confinement. Here, we consider the schemes illustrated in figure 1, for an infinite SiO_2 cylindrical waveguide of radius $a = 250$ nm. In all configurations, the beams are linearly polarized at the waveguide input to ensure azimuthal confinement for trapped atoms. A pair of x-polarized red-detuned beams generates a 1D lattice along the fiber axis for longitudinal confinement. Figure 1(b) shows the configuration used in [6], namely a pair of red-detuned, x-polarized beams and a single blue-detuned, y-polarized beam. An alternative scheme would be to use the three beams with parallel polarizations, as illustrated in figure 1(c). This scheme allows for the use of lower power for the blue-detuned beam, by approximately a factor of three for the parameters we will consider in section 3, but results in larger vector shifts, as we will discuss in the next sections. The scheme we propose makes use of four beams with parallel linear input polarizations, as shown in figure 1(d). The additional blue-detuned beam compensates for the vector shifts of its companion blue-detuned beam, as we will show.

Figure 2 illustrates a trap generated using the configuration of figure 1(b) and the parameters of [6]. About 2000 atoms were trapped in a 1D lattice with a 50 ms lifetime. This advance achieved by the group of A Rauschenbeutel represents an important milestone towards the micro-manipulation of ultra-cold atoms using evanescent field traps.

2.3. HE$_{11}$ mode—electric field polarization

The fundamental mode HE$_{11}$ is often referred to as 'quasi-linear' when excited with a linearly polarized input beam. However, for a dielectric waveguide in the strong-guiding regime with indices of refraction $n_1 \approx 1.5$ inside the waveguide and $n_2 \approx 1.0$ outside, the HE$_{11}$ mode actually exhibits a significant ellipticity for $a \lesssim \lambda/2$, leading to vector shifts of the Zeeman sublevels. Formally, for a linearly polarized input, the evanescent field $\mathbf{E} = (E_x, E_y, E_z)$ of the fundamental mode propagating in the fiber can be expressed as follows for $r \geqslant a$ [7, 44, 45]:

$$E_x(r, \phi, z, t) = A_{\text{lin}} \frac{\beta_{11} J_1(h_{11}a)}{2q_{11}K_1(q_{11}a)}[(1 - s_{11})K_0(q_{11}r)\cos(\varphi_0)$$

$$+(1 + s_{11})K_2(q_{11}r)\cos(2\phi - \varphi_0)]e^{i(\omega t - \beta_{11}z)}, \tag{4a}$$

$$E_y(r, \phi, z, t) = A_{\text{lin}} \frac{\beta_{11} J_1(h_{11}a)}{2q_{11}K_1(q_{11}a)}[(1 - s_{11})K_0(q_{11}r)\sin(\varphi_0)$$

$$+(1 + s_{11})K_2(q_{11}r)\sin(2\phi - \varphi_0)]e^{i(\omega t - \beta_{11}z)}, \tag{4b}$$

$$E_z(r, \phi, z, t) = iA_{\text{lin}} \frac{J_1(h_{11}a)}{K_1(q_{11}a)}K_1(q_{11}r)\cos(\phi - \varphi_0)e^{i(\omega t - \beta_{11}z)}, \tag{4c}$$

a) U_{trap} (mK)   **b)**
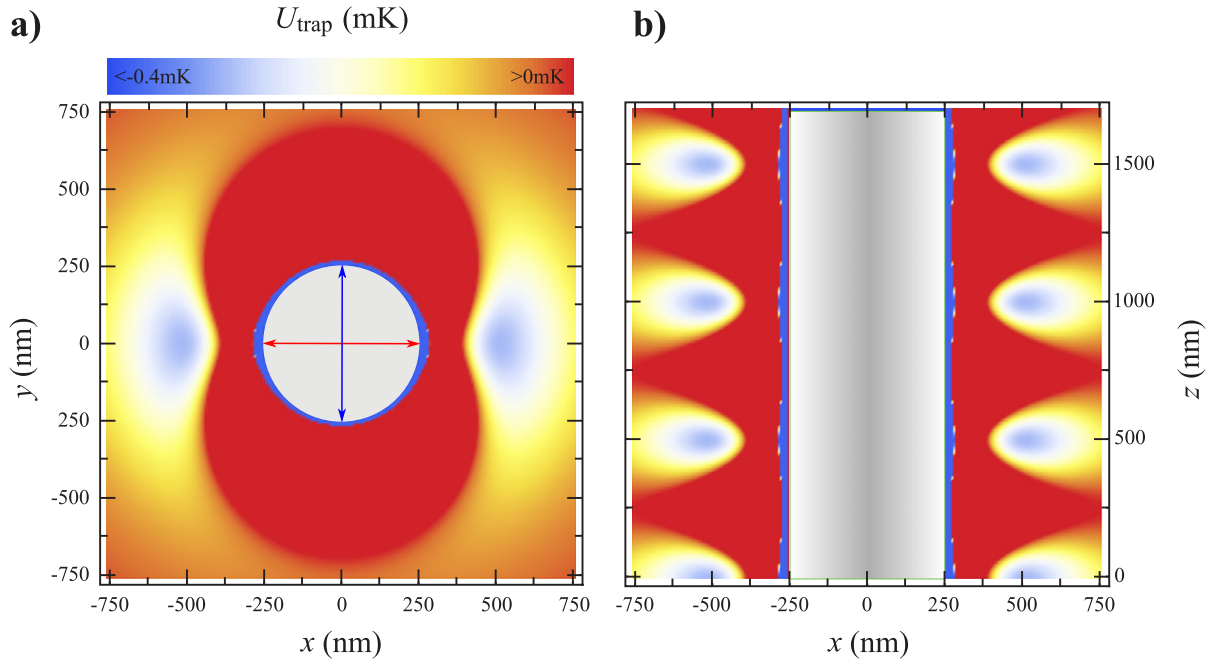
Figure 2. A ground-state trapping potential U_{trap} is generated by two orthogonally polarized evanescent fields, confining Cs atoms outside a 500 nm diameter optical fiber. Input polarizations are denoted by the arrows. (a) $x–y$ plane. (b) $x–z$ plane. U_{trap} results from two counter-propagating red-detuned beams (1064 nm, 2×2.2 mW), and a single blue-detuned beam (780 nm, 25 mW), as shown in figure 1(b) [6]. The standing wave structure of the attractive red-detuned field and the repulsive force from the blue-detuned beam enable 3D confinement of Cs atoms at each minimum of U_{trap} near the dielectric waveguide. U_{trap} diverges as the surface is approached due to the attractive van der Waals force.
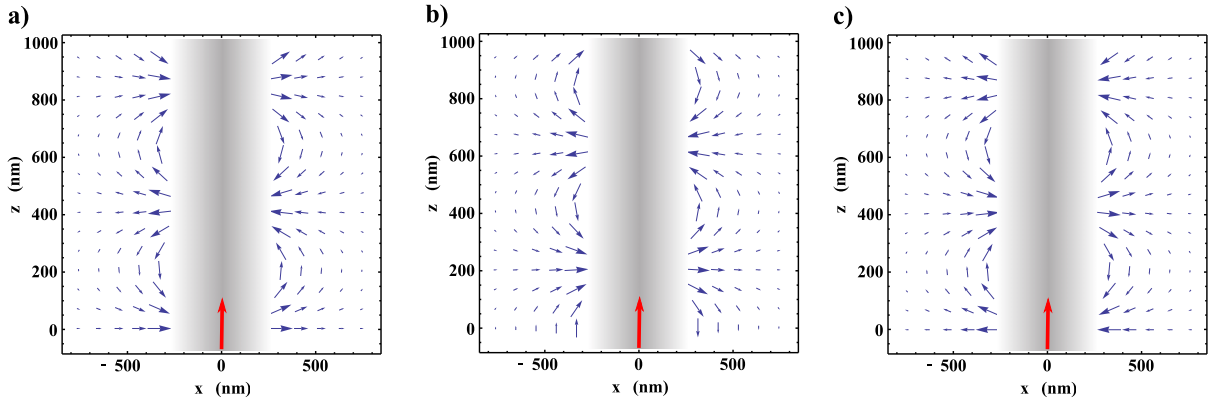
with

$$s_{11} = \left[\frac{1}{(h_{11}a)^2} + \frac{1}{(q_{11}a)^2} \right] \left[\frac{J_1'(h_{11}a)}{h_{11}a\,J_1(h_{11}a)} + \frac{K_1'(q_{11}a)}{q_{11}a\,K_1(q_{11}a)} \right], \tag{5a}$$

$$h_{11} = \sqrt{k_0^2 n_1^2 - \beta_{11}^2}, \tag{5b}$$

$$q_{11} = \sqrt{\beta_{11}^2 - k_0^2 n_2^2}. \tag{5c}$$

Here, ϕ denotes the azimuthal position in the transverse plane (figure 1(a)), φ_0 indicates the polarization axis for the input polarization relative to the x axis, n_1 and n_2 are the indices of refraction inside and outside the waveguide, β_{11} is the mode propagation constant, $1/h_{11}$ is the characteristic decay length for the guided mode inside the fiber, $1/q_{11}$ is the characteristic decay length for the guided mode outside the fiber, A_{lin} is the real-valued amplitude for the linearly polarized input, J_l is the lth Bessel function of the first kind and K_l is the lth modified Bessel function of the second kind.

Figure 3. Electric field $\mathbf{E}(x, y, z, t)$ of a single propagating beam in the plane $y = 0$. The input beam is x-polarized. The electric field $\text{Re}[\mathbf{E}(x, y, z, t)]$, with $\mathbf{E}(x, y, z, t)$ defined as in equation (4), is indicated by the blue arrows. The red arrow indicates the beam propagation direction. The field is shown for (a) $\omega t = 0$, (b) $\omega t = \pi/2$ and (c) $\omega t = \pi$.

It is clear from equation (4) that the electric field intensity is not azimuthally symmetric. For a beam polarized along $\mathbf{e}_x$, i.e. $\varphi_0 = 0$, the intensity at the fiber's outer surface is maximum for $\phi = 0, \pi$ and minimum for $\phi = \pm\pi/2$.

Notably, the evanescent modes of the nanofiber have a significant longitudinal component E_z along the fiber propagation direction, which is $\pi/2$ out-of-phase with the transverse components (E_x, E_y) (equation (4c)). At the outer fiber surface, E_z is maximum for $\phi = \varphi_0, \varphi_0 + \pi$ (i.e. along the input polarization axis) and vanishes for $\phi = \varphi_0 \pm \pi/2$. For an x-polarized input at 937 nm and a nanofiber of radius $a = 250$ nm, $\frac{|E_z|^2}{|E|^2}$ $(r = a_+, \phi = 0) \simeq 20\%$. As a consequence, the polarization of a single propagating beam will be elliptical everywhere except for $\phi = \varphi_0 \pm \pi/2$. The ellipticity of the beam will be maximum for $\phi = \varphi_0, \varphi_0 + \pi$ as is illustrated in figure 3, giving rise to significant vector shifts, which we describe in section 3.

We can re-write equations (4) as follows:

$$E_x(r, \phi, z, t) = A\, e^{i(\omega t - \beta_{11} z)}, \tag{6a}$$

$$E_y(r, \phi, z, t) = B\, e^{i(\omega t - \beta_{11} z)}, \tag{6b}$$

$$E_z(r, \phi, z, t) = iC\, e^{i(\omega t - \beta_{11} z)}, \tag{6c}$$

where A, B and C are real functions of r and ϕ. In particular, if one combines a forward-propagating beam $\mathbf{E}^{(\text{fwd})}$ expressed as equation (6) with a backward-propagating beam of the same amplitude and input polarization $\mathbf{E}^{(\text{bwd})} = A\, e^{i(\omega t + \beta_{11} z)}\mathbf{e}_x + B\, e^{i(\omega t + \beta_{11} z)}\mathbf{e}_y - i\, C\, e^{i(\omega t + \beta_{11} z)}\mathbf{e}_z$, the total field can be expressed as

$$\mathbf{E}^{(\text{tot})} = \mathbf{E}^{(\text{fwd})} + \mathbf{E}^{(\text{bwd})} = 2\left[A\cos(\beta_{11} z)\mathbf{e}_x + B\cos(\beta_{11} z)\mathbf{e}_y + C\sin(\beta_{11} z)\mathbf{e}_z \right] \cdot e^{i\omega t}. \tag{7}$$

The resulting electric field $\mathbf{E}^{(\text{tot})} = \mathbf{E}^{(\text{fwd})} + \mathbf{E}^{(\text{bwd})}$ forms an optical lattice with spatially rotating linear polarization as illustrated in figure 4. In particular, the polarization state of the field rotates between the pure linear x- and z-polarizations along z at $\phi = 0$, as illustrated in figure 5.
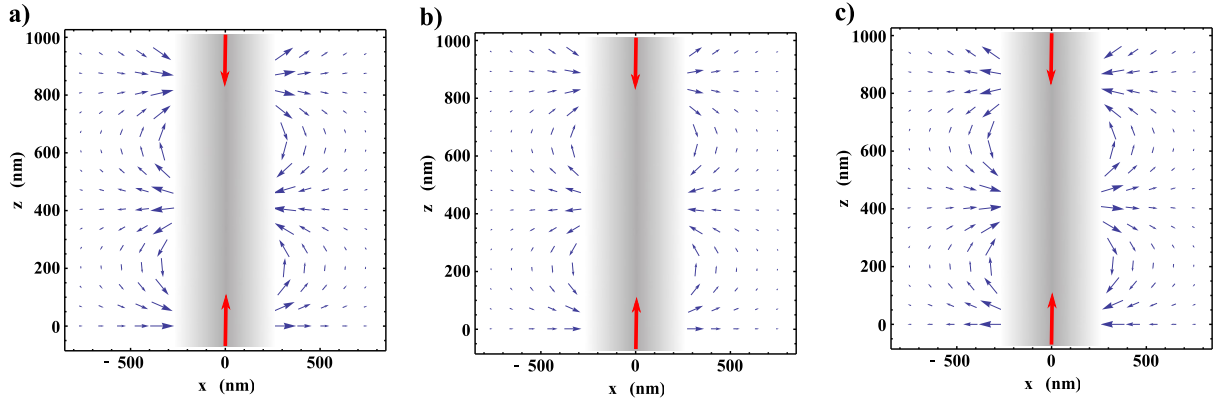
Figure 4. Total electric field $\mathbf{E}(x, y, z, t)$ for two counter-propagating beams in the plane $y = 0$. The input beams are x-polarized. The electric field $\mathrm{Re}[\mathbf{E}(x, y, z, t)]$ is indicated by the blue arrows. The red arrows indicate the beam propagation directions. The electric field is shown for (a) $\omega t = 0$, (b) $\omega t = \pi/4$ and (c) $\omega t = \pi$. As opposed to figure 3, the polarization of the electric field is linear at any point $|\mathbf{r}| > a$ (i.e. the polarization vector has no ellipticity and $\mathbf{E}$ does not rotate in time at a given position $\mathbf{r}$ as in 3).
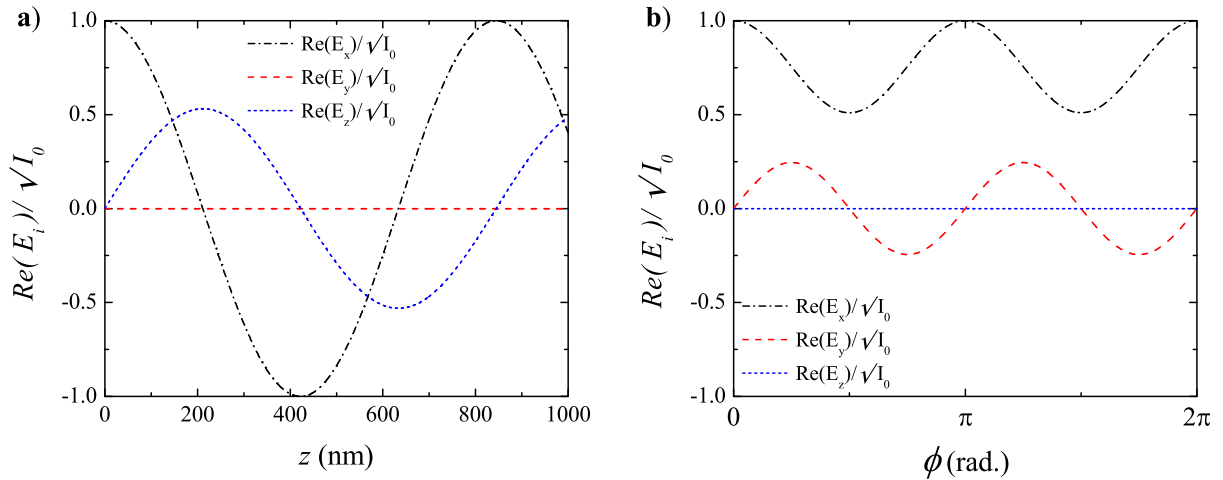
Figure 5. Electric field amplitude after interference $\mathbf{E}^{(\mathrm{tot})} = \mathbf{E}^{(\mathrm{fwd})} + \mathbf{E}^{(\mathrm{bwd})}$ of two 937 nm beams with $\delta_{fb} = 0$, at $t = 0$ and $r = a_+$ as in figure 1(d) (i.e. x-polarized inputs with $\varphi_0 = 0$). The fields are normalized to the intensity I_0 at $r = a_+$, $\phi = 0$, $z = 0$. (a) The axial direction z (at $\phi = 0$). (b) The azimuthal direction ϕ (at $z = 0$). In particular, $\mathbf{E}^{(\mathrm{tot})}$ has a fixed linear polarization at any given point $\mathbf{r}$ which rotates as $\mathbf{r}$ is varied.

2.4. Cancellation of the vector shifts

In [6], the properties shown in figures 4 and 5 were used to cancel the vector shifts of ground and excited m_F states in Cs for the pair of red-detuned trapping beams for the configuration in figure 1(b). However, vector shifts due to the single blue-detuned beam were zero only for

$\phi = \varphi_0,\ \varphi_0 + \pi$. Although the atoms are trapped at $\phi = \varphi_0,\ \varphi_0 + \pi$, inevitable fluctuations of the atom position will lead to non-zero vector light shifts of both ground and excited states.

The scheme in figure 1(c) allows for the use of reduced power for the blue-detuned beams as compared to figure 1(b) but with the consequence of large vector shifts from the ellipticity of the electric field even for $\phi = 0$. We will therefore not consider this scheme in the next sections.

By contrast, the vector shifts of both the ground and excited states can be canceled for both the red and blue-detuned fields by using pairs of counter-propagating beams, as shown in figure 1(d). In the x–z plane, the vector shift for each pair becomes $\hat{H}_1 \propto (\alpha^{(1)}(\omega^{\text{(fwd)}}) - \alpha^{(1)}(\omega^{\text{(bwd)}}))\frac{\hat{F}_y}{F}$ with $\omega^{\text{(fwd)}} \simeq \omega^{\text{(bwd)}}$, where $\omega^{\text{(fwd,bwd)}}$ are the angular frequencies for the forward and backward propagating beams, and $\delta \pm \delta_{fb}/2$ are their detunings from the atomic transition frequency ω_{a}, with two-photon detuning $\delta_{fb} = \omega^{\text{(fwd)}} - \omega^{\text{(bwd)}}$. For an atom in the x–z plane, the total electric field is also contained in the x–z plane, such that the scalar product $(\hat{\mathbf{E}}^{(-)} \times \hat{\mathbf{E}}^{(+)}) \cdot \hat{\mathbf{F}}$ in equation (2) is proportional to $\hat{F}_y$.

In the case of the red-detuned lattice, $\omega_{\text{red}}^{\text{(fwd)}} = \omega_{\text{red}}^{\text{(bwd)}}$ and $\hat{H}_1^{\text{(red)}} = 0$, precisely as in [6]. Adding a blue-detuned lattice with $\delta_{fb} = 0$ would result in two superimposed lattices with unmatched spatial periods $2\pi/\beta_{11}^{\text{red}}$, $2\pi/\beta_{11}^{\text{blue}}$. To avoid this effect, the interference between the counter-propagating blue-detuned fields $\mathbf{E}_{\text{blue}}^{\text{(fwd)}}$ and $\mathbf{E}_{\text{blue}}^{\text{(bwd)}}$ can be averaged over times short compared to the time scale of the motional and internal dynamics of a trapped atom by offsetting the frequencies of the two fields by $\delta_{fb} \gg (\omega_{\text{trap}}, \delta_{\text{hfs}})$, where ω_{trap} and δ_{hfs} are the trap angular frequency and the hyperfine splitting for the ground state, respectively. This will also suppress spurious two-photon processes (e.g. two-photon Stark shift [46]), as well as parametric heating due to intensity modulation [47].

For $\omega_{\text{blue}}^{\text{(fwd,bwd)}} = \omega_{\text{a}} + (\delta \pm \delta_{fb}/2)$, we achieve a vector shift cancellation for the blue-detuned field to the first order in $1/\delta$, namely

$$\hat{H}_1^{\text{(blue)}} \propto \frac{\delta_{fb}}{\delta^2}\frac{\hat{F}_y}{F} + \mathcal{O}(1/\delta^3). \tag{8}$$

For typical values of $\delta = 85\,\text{THz}$ and $\delta_{fb} = 30\,\text{GHz}$, $\delta_{fb}/\delta = 3.5 \times 10^{-4}$.

2.5. Magic wavelengths for an evanescent field trap

To make the nanofiber trap state-insensitive, it is necessary to cancel the differential scalar shift δU_{scalar} of the $6S_{1/2}$ and $6P_{3/2}$ states by operating the trap at the magic wavelengths, as proposed in [35], in which only the effects of the scalar and tensor shifts were considered. Here we deal with the full complexity of the vector field $\mathbf{E}(\mathbf{r})$ and the resulting vector light shifts. We numerically determine the red-detuned and blue-detuned magic wavelengths for the $6S_{1/2} \rightarrow 6P_{3/2}$ transition, following the procedure described in [30, 34, 48, 49]. The calculation includes the contributions of all the hyperfine levels F and Zeeman sublevels m_F of the electronic states $\{6S_{1/2}, \ldots, 15S_{1/2}\}$, $\{6P_{1/2}, \ldots, 11P_{1/2}\}$, $\{6P_{3/2}, \ldots, 11P_{3/2}\}$, $\{6D_{3/2}, \ldots, 11D_{3/2}\}$ and $\{6D_{5/2}, \ldots, 11D_{5/2}\}$. The effect of the tensor shifts on the $6P_{3/2}$ excited state is manifest in the quadratic splitting of the $m_{F'}$ sublevels (figure 6). We find a red-detuned magic wavelength located around 935 nm, in accordance with the previously published values [34, 49]. In the next sections, we will use the value $\lambda_{\text{red}} = 937$ nm, which cancels δU_{scalar} for the $6P_{3/2}$ excited state $|F' = 4, m_{F'} = 0\rangle$. We choose $F' = 4$ due to its relevance for coherent two-photon processes [15–17]. There are several blue-detuned magic wavelengths [35, 49]. For our trap, we use the magic wavelength λ_{blue} at approximately 687 nm [35]. Since this is the second closest
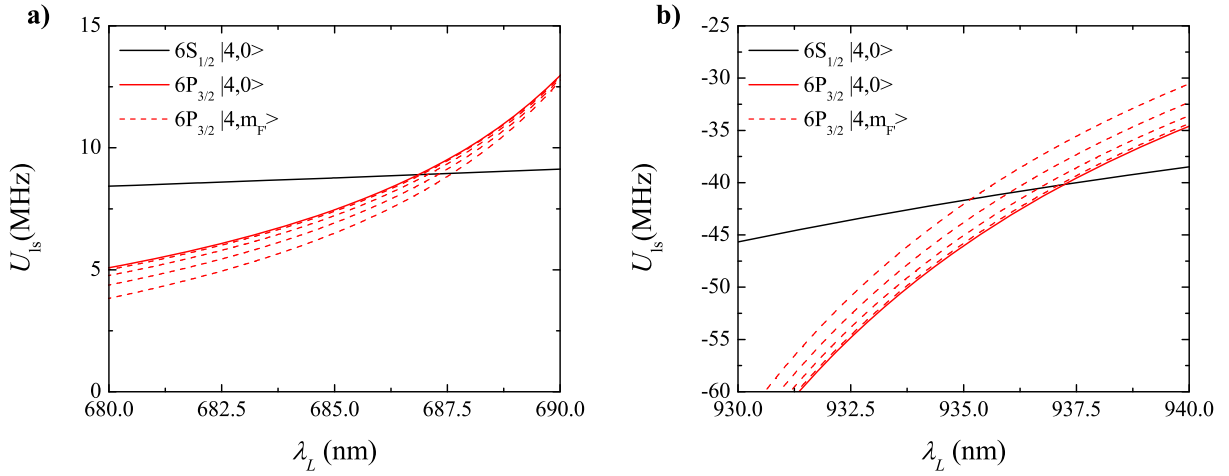
Figure 6. Magic wavelengths of the Cs D_2 line. We display the light shift U_{ls} for a linearly polarized beam with constant intensity $2.9 \times 10^9 \, \mathrm{W \, m^{-2}}$ around (a) the blue-detuned magic wavelength at $\lambda_{blue} \simeq 687 \, \mathrm{nm}$ and (b) red-detuned magic wavelength at $\lambda_{red} \simeq 937 \, \mathrm{nm}$.

blue-detuned magic wavelength to 852 nm, it has the second highest ground-state polarizability and therefore requires the second lowest optical intensity to generate the required trapping potential (we do not consider the magic wavelength at 792 nm, as it is too close to the $8S_{1/2}$ to $6P_{3/2}$ transitions at 794 nm).

We have neglected higher-order processes in our analysis, including two-photon and electric quadrupole transitions, near 687 nm [50].

3. Numerical results: trapping potentials

Using the atomic interaction Hamiltonian in the dipole approximation with the actual polarization profile of the evanescent field, we proceed to analyze the adiabatic potentials for the nanofiber trap for a Cs atom in its $6S_{1/2}$ ground and $6P_{3/2}$ excited states.

3.1. Total potential

For a specific atomic state of Cs, the total atomic trap potential U_{trap} consists of the total light-shift potential U_{ls} calculated from the full-Stark shift Hamiltonian (equation (2)), as well as the surface interaction potential of an atom with the dielectric waveguide $U_{surface}$, namely

$$U_{trap} = U_{ls} + U_{surface}. \tag{9}$$

The Casimir–Polder interaction between the atom and dielectric surface has a significant effect on the atomic motion at distance scales near 100 nm [20, 51–54]. The surface potential of a ground-state Cs atom near a planar dielectric surface can be reasonably approximated by the van der Waals potential which decays as d^{-3}, where $d = r - a$:

$$U_{surface} = -\frac{C_3}{d^3}, \tag{10}$$

where we use $C_3(6S_{1/2})/h = 1.16\,\text{kHz}\,\mu\text{m}^3$ [21]. Because the retarded Casimir–Polder forces (d^{-4} scaling) decrease faster away from the surface than the van der Waals forces, using U_{surface} overestimates the surface interaction at the trap location $d \approx 200\,\text{nm}$. Additionally, the curvature of the nanofiber cylindrical geometry reduces the potential strength even further [21, 55]. The d^{-3} scaling of the van der Waals expression for a planar surface is therefore an overestimate of the actual surface potential. We use it for simplicity in the calculations presented here, with more complete expressions for Cs presented in [21]. Furthermore, we neglect any dependence on the $m_{F'}$ sublevels of the excited state $6P_{3/2}$, and simply approximate $C_3(6P_{3/2}) \approx 2\,C_3(6S_{1/2})$ [56]. We estimate that the corrections added by the retarded potential and the surface curvature should be negligible at the trap location, as the surface potential falls off faster than the light potential, as further discussed in the appendix.

We calculate the adiabatic potential of equation (9) by diagonalizing the total interaction Hamiltonian $\hat{H} = \hat{H}_{\text{ls}} + \hat{H}_{\text{surface}}$ at each point in space, where $\hat{H}_{\text{surface}}$ is the scalar surface Hamiltonian. At each point $\mathbf{r}(r, \phi, z)$, we obtain a set of eigenstates and the corresponding eigenenergies. These eigenstates are superpositions of the $|F, m_F\rangle$ bare Zeeman sublevels. Due to the complex polarization of the trapping fields, the energy eigenstates are not necessarily eigenstates of any projection of the angular momentum operator.

3.2. Effect of the light shifts in a 'non-magic' trap

First, we consider the trapping parameters for the experiment of Vetsch *et al* [6]. Despite its impressive experimental success, the ground-state levels exhibit splittings that impair the ground-state coherence. In the realization of [6], the two-color evanescent trap is constructed using a pair of counter-propagating x-polarized ($\varphi_0 = 0$) red-detuned beams $\mathbf{E}_{\text{red}} = \mathbf{E}_{\text{red}}^{(\text{fwd})} + \mathbf{E}_{\text{red}}^{(\text{bwd})}$ ($P_{\text{red}} = 2 \times 2.2\,\text{mW}$) at $\lambda_{\text{red}} = 1064\,\text{nm}$, forming an optical lattice, and a single repulsive y-polarized ($\varphi_0 = \pi/2$) blue-detuned beam $\mathbf{E}_{\text{blue}}$ ($P_{\text{blue}} = 25\,\text{mW}$) at $\lambda_{\text{blue}} = 780\,\text{nm}$. The SiO_2 tapered optical fiber has a radius $a = 250\,\text{nm}$ in the trapping region.

Figure 7 shows the radial trapping potential $U_{\text{trap}}(r, \phi, z)$ of the ground states $F = 3$ and $F = 4$ of $6S_{1/2}$ and excited states $F' = 4$ of $6P_{3/2}$, for $z = 0$ and $\phi = 0$ (x-axis) (figure 7(a) and for $\phi = \pi/2$ (y-axis) figure 7(b)). The energy sublevels of the ground states at the trap location ($\phi = 0$) are degenerate, as both trapping fields are linearly polarized as illustrated in figure 4. The excited state energy sublevels are shifted due to the vector and tensor shifts. The trap depth for the ground state is $U_{\text{depth}} = -0.4\,\text{mK}$, located at $r - a \simeq 230\,\text{nm}$ and $\phi = 0$, whereas the excited states are not trapped at all.

The azimuthal dependence of the trap potential reveals a significant inhomogeneous broadening of the energy sublevels due to the ellipticity of $\mathbf{E}_{\text{blue}}$ for $\phi \neq 0, \pi$ (figure 8). To estimate this broadening, we assume that the potential is harmonic around the trap minimum. By fitting the ground state $F = 3$ potential with a harmonic potential around $\phi = \pi$, we obtain an azimuthal trapping frequency $\nu_{\text{trap}_\phi} \simeq 150\,\text{kHz}$. For an atom in its azimuthal motional ground state $|n\rangle_\phi = |0\rangle_\phi$ in such a potential, the half-width σ_{r_ϕ} of the corresponding single-atom distribution is given by $\sigma_{r_\phi} = \langle (r\phi)^2 \rangle \simeq r_{\text{trap}}\sigma_\phi = \sqrt{\frac{\hbar}{4\pi m \nu_{\text{trap}_\phi}}} \simeq 16\,\text{nm}$ (or azimuthal half-width of $\sigma_\phi \simeq 2^\circ$). This leads to fast decoherence of the hyperfine and Zeeman levels, even with ground-state cooling. Specifically, we estimate a spin-wave coherence time $\tau_m = 1/\delta\nu_\phi \lesssim 5\,\mu\text{s}$, derived from the $\delta\nu_\phi = 200\,\text{kHz}$ splitting between the sublevels of the $F = 4$ atomic ground state 16 nm
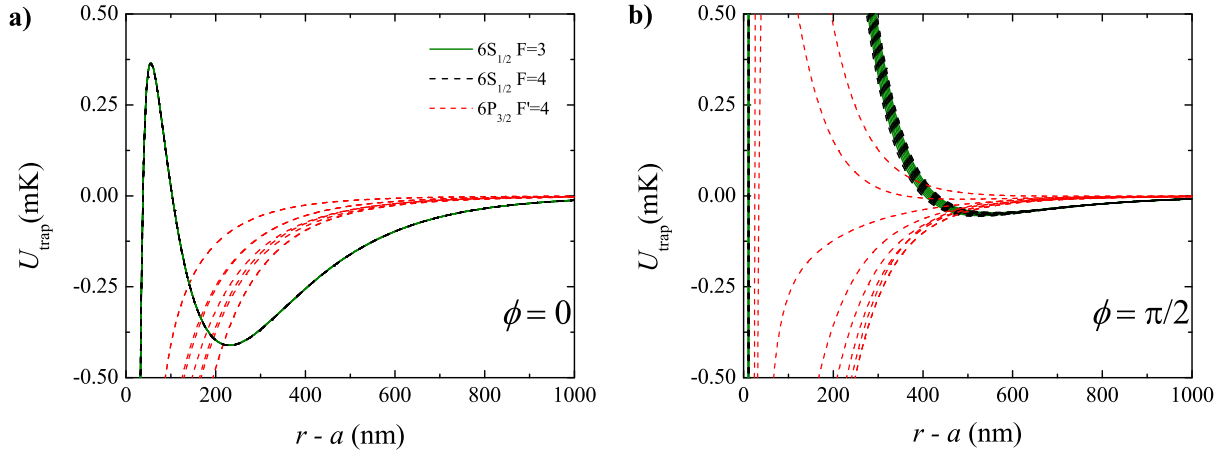
Figure 7. Radial dependence of the trapping potential of the ground and excited states for the parameters used in [6] at $z = 0$. The polarization configuration is the same as figure 1(b). The energy sublevels of the ground states $F = 3$ and $F = 4$ of $6S_{1/2}$ are shown as solid green and dashed black curves, and the $F' = 4$ sublevels of the electronically excited state ($6P_{3/2}$) are shown as red dashed curves. (a) Radial potential along $\phi = 0$. The trap minimum is located at about 230 nm from the fiber surface. The excited state is untrapped, and split by the tensor shifts. (b) Radial potential along $\phi = \pi/2$. Both ground and excited states are not trapped. The ground states exhibit a splitting due to the vector shifts induced by the elliptical polarization of the blue-detuned light, and the excited states are shifted by the vector and tensor shifts.

away from the trap minimum. This is significantly limited compared to the quantum memory performances of atomic ensembles in optical lattices (see, e.g., [57]).

Finally, we plot in figure 9 a cross-section of the axial potentials showing the axial confinement of the ground and excited states.

The excited states are untrapped in all directions except along the fiber axis z for the parameters of [6]. An atom excited to these untrapped potentials will experience dipole-force fluctuations, leading to heating [29] and preventing near-resonant driving of the optical transition [58].

3.3. State-insensitive trapping potential

We now analyze our proposed 'magic compensation' scheme (as illustrated in figure 1(d)), demonstrating how using magic wavelength beams and compensating for the trap ellipticity can reduce the inhomogeneous broadening of the Zeeman sublevels in a nanofiber trap. For this trap, we use a pair of counter-propagating x-polarized ($\varphi_0 = 0$) red-detuned beams $\mathbf{E}_{\mathrm{red}} = \mathbf{E}_{\mathrm{red}}^{(\mathrm{fwd})} + \mathbf{E}_{\mathrm{red}}^{(\mathrm{bwd})}$ ($P_{\mathrm{red}} = 2 \times 0.95\,\mathrm{mW}$) at the 'magic' wavelength $\lambda_{\mathrm{red}} = 937\,\mathrm{nm}$, forming a 1D optical lattice. Counter-propagating, x-polarized blue-detuned beams at the second 'magic' wavelength $\lambda_{\mathrm{blue}} = 687\,\mathrm{nm}$ are used with a power $P_{\mathrm{blue}} = 2 \times 16\,\mathrm{mW}$. The resulting interference is averaged out by detuning the beams by $\delta_{fb} = 30\,\mathrm{GHz}$, as explained in section 2.4, leading to a first-order cancellation of vector light shifts as expressed by equation (8). The beam intensities are chosen to generate a trap of similar depth as the one demonstrated in [6]. The resulting
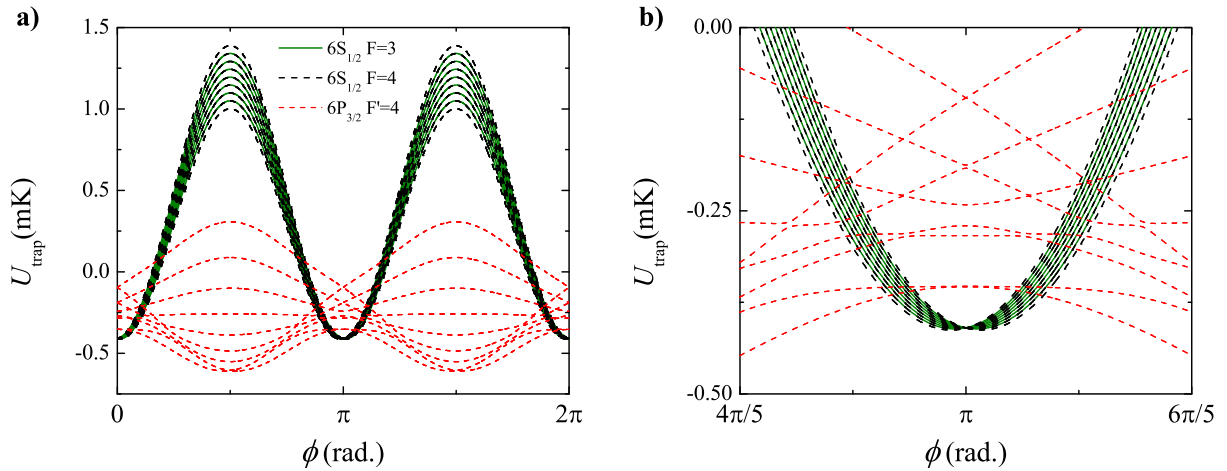
Figure 8. Azimuthal dependence of the trapping potential of the ground and excited states for the scheme in figure 1(b) and for the parameters used in figure 7. $r - a = 230$ nm and $z = 0$. (a) The ground-state splitting is minimum for $\phi = 0$ and $\phi = \pi$. Everywhere else, the polarization of the blue-detuned field induces large vector shifts. (b) Expanded view of (a) near a trap minimum at $\phi = \pi$. The Zeeman-like splitting of the ground states is large even for small azimuthal angles. The excited-state level structures are greatly altered by the combined vector and tensor shifts.
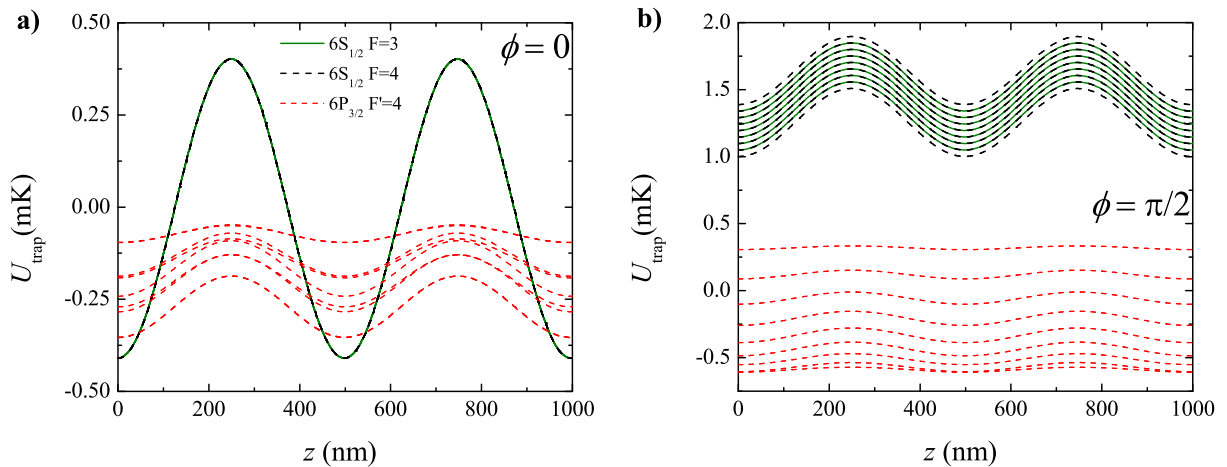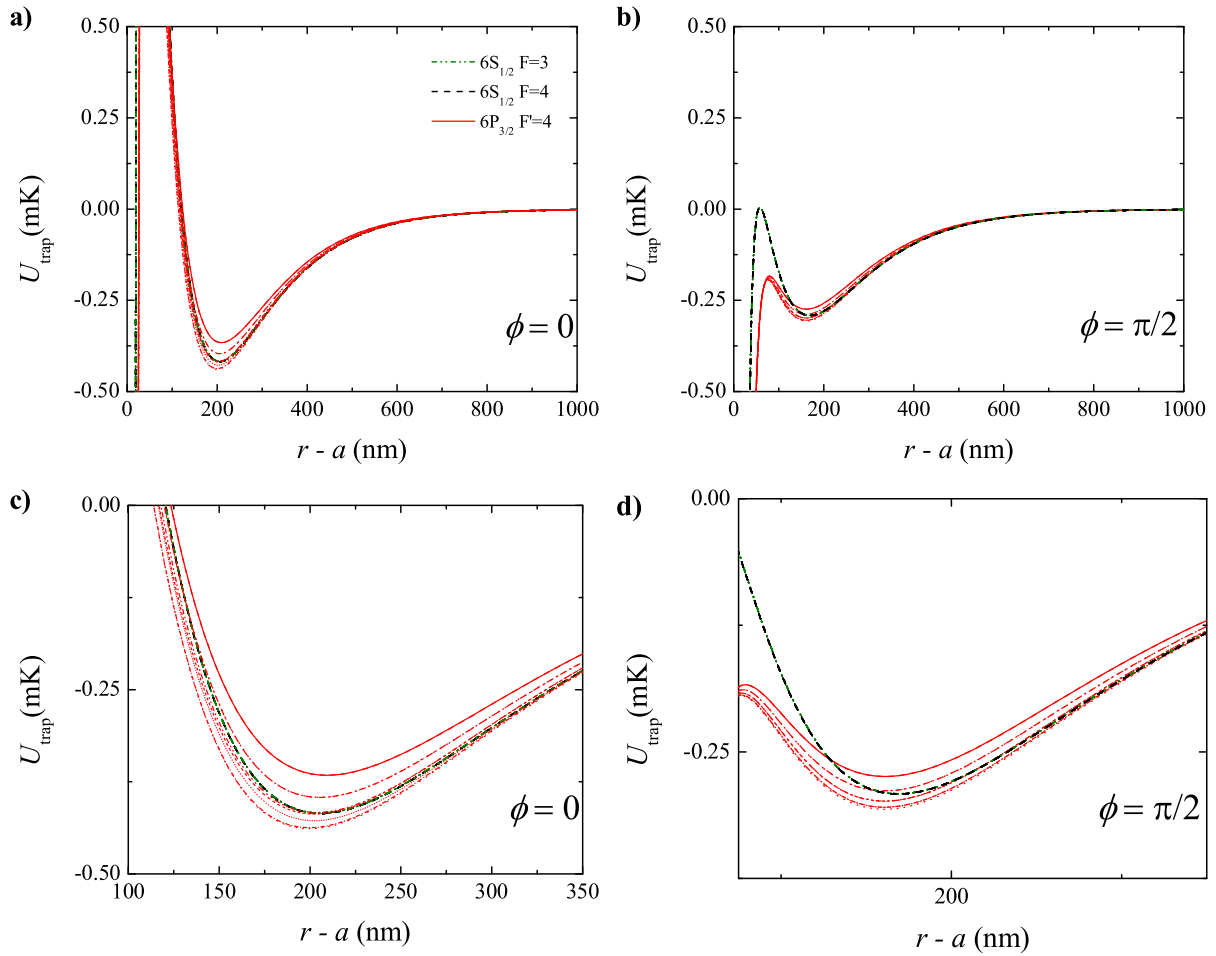

Figure 9. Axial dependence of the trapping potential for the ground and excited states for the scheme in figure 1(b) and for the parameters used in figure 7. (a) Longitudinal potential along $\phi = 0$. The distance from the fiber surface is set to $r - a = 230$ nm at the trap minimum. (b) Longitudinal potential along $\phi = \pi/2$. The distance from the fiber surface is again set to 230 nm.

adiabatic potential U_{trap} allows for state-insensitive 3D confinement of cold Cs atoms around an SiO$_2$ nanofiber of radius $a = 250$ nm.

In figure 10, we show the radial trapping potential $U_{\text{trap}}(r, \phi, z)$ of the ground and excited states for $z = 0$, $\phi = 0$ (x-axis) (figure 10(a)) and for $z = 0$, $\phi = \pi/2$ (y-axis) (figure 10(b)).
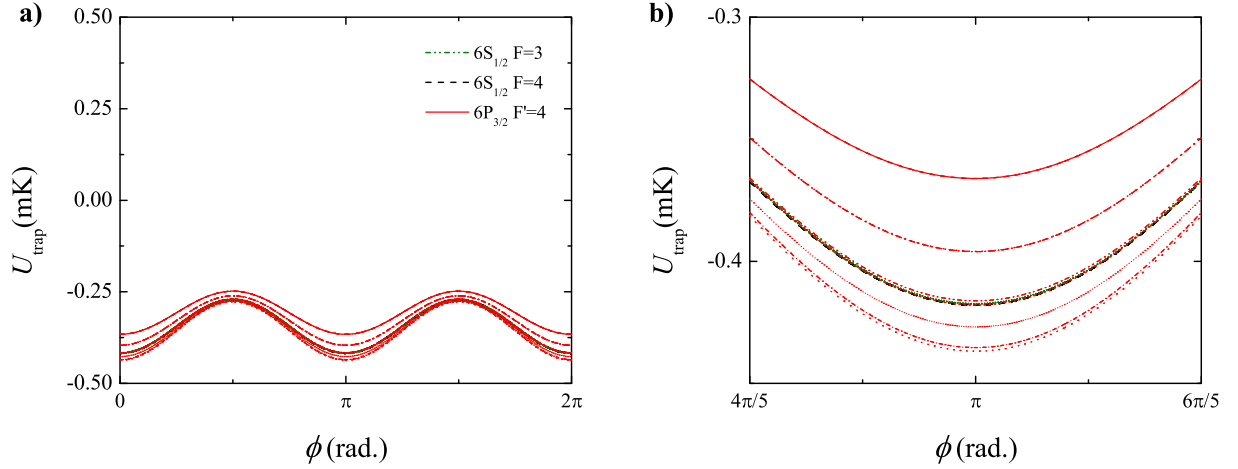
Figure 10. Radial dependence of the trapping potentials of the ground and excited states using the magic wavelengths and the configuration shown in figure 1(d). All beams are polarized along $\phi = 0$ (i.e. $\varphi_0 = 0$). The 937 nm beams each have a power of 0.95 mW. The 687 nm beams each have a power of 16 mW. (a) Radial potentials along $\phi = 0$ (i.e. $\varphi_0 = 0$). The trap minimum for $6S_{1/2}$ is located at about 210 nm from the fiber surface. Both electronic ground and excited states are trapped, with residual splittings of the excited states due to the tensor shifts. (b) Radial potential along $\phi = \pi/2$. (c, d) Expanded views of (a) and (b) around the trap minimum.

Because the trapping fields are now effectively linearly polarized, the ground states are degenerate at both $\phi = 0$ and $\phi = \pi/2$. In contrast to a non-magic wavelength trap, the excited states are trapped with gradients that closely map that of the ground states. The sublevels of $6P_{3/2}$ are still non-degenerate due to the tensor shifts. For P_{red}, P_{blue} specified above, we find that the trap depth is $U_{depth} = -0.4$ mK, located at $r - a \simeq r_{trap} - a = 210$ nm and $\phi = 0, \pi$.

The azimuthal confinement of the atoms is shown by figure 11. The trap depth is reduced compared to figure 8, due to the use of parallel polarizations for the trapping beams. This could be overcome by using higher trapping power, to make the trap deeper in all directions. Using perpendicular polarizations for the blue-detuned and red-detuned beams would unfortunately

Figure 11. (a) Azimuthal dependence of the trapping potential of the ground and excited states for the 'magic compensated' trap (figure 1(d)) with the parameters used in figure 10, for $r - a = 210$ nm. (b) Expanded view of (a) around a trap minimum. The effect of the compensation beam in figure 1(d) is to suppress the vector shifts and to reduce the ground-state splittings $\delta \nu_\phi$ in the transverse plane for $\phi \neq 0, \pi$.

require prohibitively high power at 685 nm. In contrast to the configurations shown in figures 1(b) and (c), the inhomogeneous Zeeman broadening from the ellipticity of $\mathbf{E}_{\text{blue}}$ is greatly reduced thanks to the compensation scheme of figure 1(d). It is non-zero, however, as expressed by equation (8). The remaining splitting of the $F = 4$ ground state is $\delta_\nu \approx 700$ Hz, limiting the coherence time to $\tau \lesssim 1/\delta_\nu = 1.4$ ms.

In the case of perfect cancellation of the vector shift with $\delta_{fb} = 0$, a residual non-zero ground-state splitting $\delta \nu_\phi$ would still arise from the different scalar dynamic polarizabilities of the $6S_{1/2} F = 3$ and $F = 4$ ground states [59]. For atoms in their azimuthal motional ground state $|n\rangle_\phi = |0\rangle_\phi$, the single-atom distribution half-width is $\sigma_{r_\phi} \simeq 30$ nm (or $\sigma_\phi \simeq 4°$) with azimuthal trap frequency $\nu_{\text{trap}_\phi} \simeq 44$ kHz obtained from a harmonic fit of the potential around $\phi = \pi$. We estimate a spin-wave coherence time $\tau_m = 1/\Delta(\delta \nu_\phi) \lesssim 30$ ms, coming from the spread $\Delta(\delta \nu_\phi) = \delta \nu_\phi(\phi = \pi) - \delta \nu_\phi(\phi = \pi + \sigma_\phi) \approx 30$ Hz of the atomic ground states for the $F = 3 \rightarrow F = 4$ transition frequency.

We note that the longest achievable coherence time in the 'magic compensated' adiabatic potential in the absence of ground-state splitting $\delta \nu_\phi$ would be limited by spontaneous Raman scattering driven by the trapping beams [34].

Finally, we also plot the axial potentials in figure 12, showing the confinement for both the ground and excited states.

Thanks to the use of the magic wavelengths, the excited states are trapped in all directions. This results in greatly suppressed dipole-force fluctuations, allowing for on-resonance driving of the optical transition.

4. Conclusion

We have proposed and analyzed in detail a scheme for a state-insensitive optical nanofiber trap that utilizes realistic experimental parameters. The 'magic' trapping wavelengths of 937
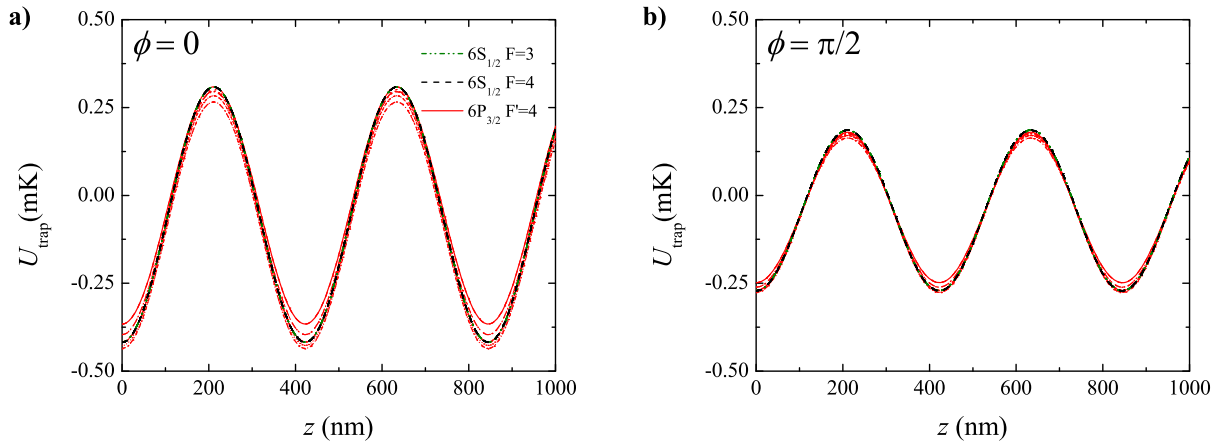
Figure 12. Axial dependence of the trapping potentials of the ground and excited states for the 'magic compensated' trap (figure 1(d)) with the parameters used in figure 10. (a) Longitudinal potential along $\phi = 0$ for $r - a = 210$ nm. (b) Longitudinal potential along $\phi = \pi/2$ for $r - a = 210$ nm.

and 687 nm for Cs atoms are readily available using semiconductor laser sources, and require a reasonable power for trapping. Tapered optical fibers can be made with sub-wavelength diameters and high transmission, as has been demonstrated experimentally [60, 61]. In [62] we describe an experiment for trapping Cs using figure 1(d) configuration and explicitly demonstrate features of the 'compensated magic' trap for a nanofiber.

Furthermore, extension to other nanoscopic dielectric waveguides [63] would make evanescent optical trapping possible in integrated hybrid quantum devices [64]. It is worth noting that the compensation scheme of the vector shift would work at any wavelength, increasing the ground-state coherence time in a straightforward manner.

The proposed 'magic compensated' scheme allows for in-trap resonant processes, increasing the trap lifetime under near-resonant driving of the transition, such as optical pumping. The scattering rate in this trap is similar to the one obtained with the parameters of [6], but the mismatch between the ground and excited states potentials could lead to the large heating in [6]. However, it is not clear whether the 'magic compensated' trap will be more robust to experimental fluctuations, and experimental studies will be required to investigate the possible limitations of the trap lifetime. An important advantage of the proposed scheme is the large reduction of the splitting of the ground-state manifolds compared to the scheme used in [6], therefore leading to increased ground-state coherence time. These properties will make quantum-state engineering more feasible in such a trap, allowing for a wide range of experiments including creating quantum memories, coupling of single atoms and ensembles to optical or mechanical resonators and studying 1D spin chains.

Acknowledgments
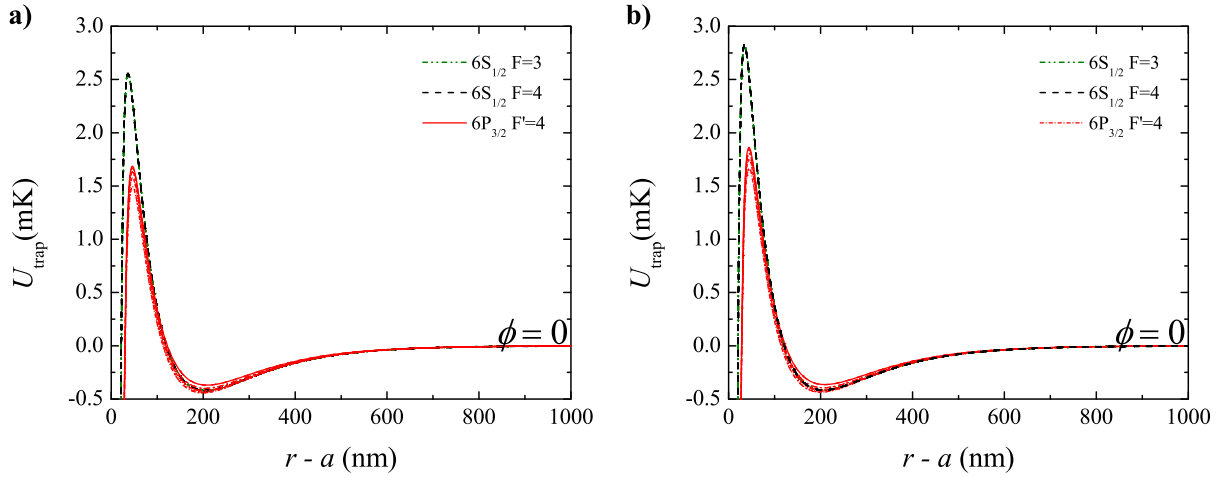
Figure A.1. Radial potential obtained using (a) the van der Waals surface potential $U_{surface} = -C_3/d^3$ and (b) the heuristic surface potential of equation (A.1). There is no noticeable difference at the potential minimum on this scale.

Appendix. Effect of the surface potential at the trap location

The expression used in our calculation for the surface potential is an approximation, and we attempt here to give an estimate of the error caused by this approximation at the trap location. We will consider two main aspects: firstly, the importance of the knowledge of the C_3 coefficient in equation (10); secondly, the correction added by the $1/d^4$ dependence of the Casimir–Polder potential.

We will therefore compare the radial potential presented in section 3.3 to a potential computed using the following heuristic form for the surface potential:

$$U_{surface}^{(CP)} = -C_3 \frac{f}{(d+f)d^3}, \tag{A.1}$$

where $f = C_4/C_3$. The values of C_3 and C_4 are computed for the limiting case of a Cs atom near a plane dielectric surface, as described in [21]. The values we use are: $C_3(6S_{1/2})/h = 1.16 \, kHz \, \mu m^3$, $C_4(6S_{1/2})/h = 0.15 \, kHz \, \mu m^4$, $C_3(6P_{3/2})/h = 2 \, C_3(6S_{1/2})/h$ and $C_4(6P_{3/2})/h = 0.62 \, kHz \, \mu m^4$. Please note that the C_3 value for the excited state from [21] is $C_3(6P_{3/2})/h = 1.71 \, kHz \, \mu m^3$.

Figure A.1 shows the potential presented in the main text and the potential obtained using the above expression. The main noticeable difference is the height of the potential barrier around 45 nm away from the surface. The potential looks otherwise the same at the trap location on that scale.

In figure A.2, we plot the difference $\delta = U_{trap} - U_{trap}^{(CP)}$, where U_{trap} is the potential obtained using equations (9) and (10) and $U_{trap}^{(CP)}$ is the potential obtained using equation (A.1). For the ground state, the residual difference is $\approx$1% of the trap depth around the trap minimum, 210 nm away from the surface, as shown in figure A.2(a). For the excited state, this difference is $\approx$1.5% at the potential minimum.
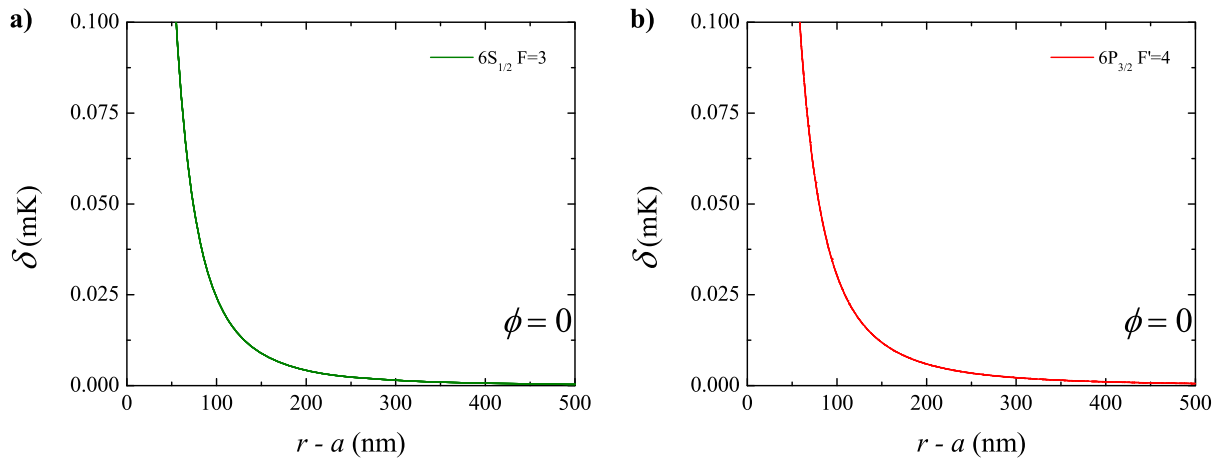
Figure A.2. The difference $\delta = U_{\text{trap}} - U_{\text{trap}}^{(\text{CP})}$ between the two potentials shown in figure A.1. (a) The ground state $F = 3$. The residual is $\approx$1% of the trap depth at the trap location. (b) The excited state $F' = 4$. The residual is $\approx$1.5% of the trap depth at the trap location.

We finally note that the curvature of the surface cannot be accounted for using the same approach as in [21], as the distance from the surface approaches the surface radius of curvature in the case of the nanofiber.

References

[1] Kimble H J 2008 The quantum internet *Nature* **453** 1023–30
[2] Renn M J, Montgomery D, Vdovin O, Anderson D Z, Wieman C E and Cornell E A 1995 Laser-guided atoms in hollow-core optical fibers *Phys. Rev. Lett.* **75** 3253–6
[3] Ito H, Nakata T, Sakaki K, Ohtsu M, Lee K I and Jhe W 1996 Laser spectroscopy of atoms guided by evanescent waves in micron-sized hollow optical fibers *Phys. Rev. Lett.* **76** 4500–3
[4] Christensen C A, Will S, Saba M, Jo G-B, Shin Y-Il, Ketterle W and Pritchard D 2008 Trapping of ultracold atoms in a hollow-core photonic crystal fiber *Phys. Rev.* A **78** 033429
[5] Bajcsy M, Hofferberth S, Balic V, Peyronel T, Hafezi M, Zibrov A S, Vuletic V and Lukin M D 2009 Efficient all-optical switching using slow light within a hollow fiber *Phys. Rev. Lett.* **102** 203902
[6] Vetsch E, Reitz D, Sague G, Schmidt R, Dawkins S T and Rauschenbeutel A 2010 Optical interface created by laser-cooled atoms trapped in the evanescent field surrounding an optical nanofiber *Phys. Rev. Lett.* **104** 203603
[7] Kien F L, Liang J Q, Hakuta K and Balykin V I 2004 Field intensity distributions and polarization orientations in a vacuum-clad subwavelength-diameter optical fiber *Opt. Commun.* **242** 445–55
[8] Nayak K P, Melentiev P N, Morinaga M, Kien F L, Balykin V I and Hakuta K 2007 Optical nanofiber as an efficient tool for manipulating and probing atomic fluorescence *Opt. Express* **15** 5431–8
[9] Sague G, Vetsch E, Alt W, Meschede D and Rauschenbeutel A 2007 Cold-atom physics using ultrathin optical fibers: light-induced dipole forces and surface interactions *Phys. Rev. Lett.* **99** 163602
[10] Balykin V I, Letokhov V S, Ovchinnikov Yu B and Sidorov A I 1988 Quantum-state-selective mirror reflection of atoms by laser light *Phys. Rev. Lett.* **60** 2137–40
[11] Cronin A D, Schmiedmayer J and Pritchard D E 2009 Optics and interferometry with atoms and molecules *Rev. Mod. Phys.* **81** 1051–129

[12] Ovchinnikov Yu B, Manek I and Grimm R 1997 Surface trap for Cs atoms based on evanescent-wave cooling *Phys. Rev. Lett.* **79** 2225–8

[13] Rychtarik D, Engeser B, Nägerl H-C and Grimm R 2004 Two-dimensional Bose–Einstein condensate in an optical surface trap *Phys. Rev. Lett.* **92** 173003

[14] Bakr W S, Peng A, Tai M E, Ma R, Simon J, Gillen J I, Folling S, Pollet L and Greiner M 2010 Probing the superfluid-to-Mott insulator transition at the single-atom level *Science* **329** 547–50

[15] Boozer A D, Boca A, Miller R, Northup T E and Kimble H J 2007 Reversible state transfer between light and a single trapped atom *Phys. Rev. Lett.* **98** 193601

[16] Choi K S, Deng H, Laurat J and Kimble H J 2008 Mapping photonic entanglement into and out of a quantum memory *Nature* **452** 67–71

[17] Hammerer K, Sorensen A S and Polzik E S 2010 Quantum interface between light and atomic ensembles *Rev. Mod. Phys.* **82** 1041–92

[18] Sangouard N, Simon C, de Riedmatten H and Gisin N 2011 Quantum repeaters based on atomic ensembles and linear optics *Rev. Mod. Phys.* **83** 33–80

[19] Aoki T, Dayan B, Wilcut E, Bowen W P, Parkins A S, Kippenberg T J, Vahala K J and Kimble H J 2006 Observation of strong coupling between one atom and a monolithic microresonator *Nature* **443** 671–4

[20] Alton D J, Stern N P, Takao Aoki, Lee H, Ostby E, Vahala K J and Kimble H J 2011 Strong interactions of single atoms and photons near a dielectric boundary *Nature Phys.* **7** 159–65

[21] Stern N P, Alton D J and Kimble H J 2011 Simulations of atomic trajectories near a dielectric surface *New J. Phys.* **13** 085004

[22] Barclay P E, Srinivasan K, Painter O, Lev B and Mabuchi H 2006 Integration of fiber-coupled high-Q SiN$_x$ microdisks with atom chips *Appl. Phys. Lett.* **89** 131108

[23] Colombe Y, Steinmetz T, Dubois G, Linke F, Hunger D and Reichel J 2007 Strong atom-field coupling for Bose–Einstein condensates in an optical cavity on a chip *Nature* **450** 272–6

[24] Trupke M, Goldwin J, Darquié B, Dutier G, Eriksson S, Ashmore J and Hinds E A 2007 Atom detection and photon production in a scalable, open, optical microcavity *Phys. Rev. Lett.* **99** 063601

[25] Zoubi H and Ritsch H 2010 Hybrid quantum system of a nanofiber mode coupled to two chains of optically trapped atoms *New J. Phys.* **12** 103014

[26] Kitagawa T, Broome M A, Fedrizzi A, Rudner M S, Berg E, Kassal I, Aspuru-Guzik A, Demler E and White A G 2011 Observation of topologically protected bound states in a one dimensional photonic system arXiv:1105.5334

[27] Shen J T and Fan S 2005 Coherent photon transport from spontaneous emission in one-dimensional waveguides *Opt. Lett.* **30** 2001–3

[28] Chang D E, Sorensen A S, Demler E A and Lukin M D 2007 A single-photon transistor using nanoscale surface plasmons *Nature Phys.* **3** 807–12

[29] Corwin K L, Kuppens S J M, Cho D and Wieman C E 1999 Spin-polarized atoms in a circularly polarized optical dipole trap *Phys. Rev. Lett.* **83** 1311–4

[30] Ye J, Kimble H J and Katori H 2008 Quantum state engineering and precision metrology using state-insensitive light traps *Science* **320** 1734–8

[31] Kimble H J 1999 *Proc. XIV Int. Conf. on Laser Spectroscopy* ed R Blatt, J Eschner, D Leibfried and F Schmidt-Kaler, vol XIV (Innsbruck, Austria: World Scientific) pp 80–9

[32] Katori H, Ido T and Kuwata-Gonokami M 1999 Optimal design of dipole potentials for efficient loading of Sr atoms *J. Phys. Soc. Japan* **68** 2479–82

[33] Ido T, Isoya Y and Katori H 2000 Optical-dipole trapping of Sr atoms at a high phase-space density *Phys. Rev.* A **61** 061403

[34] McKeever J, Buck J R, Boozer A D, Kuzmich A, Nägerl H-C, Stamper-Kurn D M and Kimble H J 2003 State-insensitive cooling and trapping of single atoms in an optical cavity *Phys. Rev. Lett.* **90** 133602

[35] Kien F L, Balykin V I and Hakuta K 2005 State-insensitive trapping and guiding of cesium atoms using a two-color evanescent field around a subwavelength-diameter fiber *J. Phys. Soc. Japan* **74** 910–7

[36] Dupont-Roc J, Polonsky N, Cohen-Tannoudji C and Kastler A 1967 Lifting of a Zeeman degeneracy by interaction with a light beam *Phys. Lett.* A **25** 87–8

[37] Felinto D, Chou C W, de Riedmatten H, Polyakov S V and Kimble H J 2005 Control of decoherence in the generation of photon pairs from atomic ensembles *Phys. Rev.* A **72** 053809

[38] Balykin V I, Hakuta K, Fam Le Kien, Liang J Q and Morinaga M 2004 Atom trapping and guiding with a subwavelength-diameter optical fiber *Phys. Rev.* A **70** 011401

[39] Dawkins S T, Mitsch R, Reitz D, Vetsch E and Rauschenbeutel A 2011 Dispersive optical interface based on nanofiber-trapped atoms *Phys. Rev. Lett.* **107** 243601

[40] Deutsch I H and Jessen P S 2010 Quantum control and measurement of atomic spins in polarization spectroscopy *Opt. Commun.* **283** 681–94

[41] Geremia J M, Stockton J K and Mabuchi H 2006 Tensor polarizability and dispersive quantum measurement of multilevel atoms *Phys. Rev.* A **73** 042112

[42] Deutsch I H and Jessen P S 1998 Quantum-state control in optical lattices *Phys. Rev.* A **57** 1972–86

[43] Chicireanu R, Nelson K D, Olmschenk S, Lundblad N, Derevianko A and Porto J V 2011 Differential light-shift cancellation in a magnetic-field-insensitive transition of ^{87}Rb *Phys. Rev. Lett.* **106** 063002

[44] Tong L, Lou J and Mazur E 2004 Single-mode guiding properties of subwavelength-diameter silica and silicon wire waveguides *Opt. Express* **12** 1025–35

[45] Sague G, Baade A and Rauschenbeutel A 2008 Blue-detuned evanescent field surface traps for neutral atoms based on mode interference in ultrathin optical fibres *New J. Phys.* **10** 113008

[46] Ashraf M M 2001 The effects of phase and Stark shift on two-photon process *J. Opt. B: Quantum Semiclass. Opt.* **3** 39–43

[47] Savard T A, O'Hara K M and Thomas J E 1997 Laser-noise-induced heating in far-off resonance optical traps *Phys. Rev.* A **56** R1095–8

[48] Katori H, Takamoto M, Pal'chikov V G and Ovsiannikov V D 2003 Ultrastable optical clock with neutral atoms in an engineered light shift trap *Phys. Rev. Lett.* **91** 173005

[49] Arora B, Safronova M S and Clark C W 2007 Magic wavelengths for the np–ns transitions in alkali-metal atoms *Phys. Rev.* A **76** 052509

[50] DiBerardino D, Tanner C E and Sieradzan A 1998 Lifetime measurements of cesium $5d^2$d$_{5/2,3/2}$ and $11s^2$s$_{1/2}$ states using pulsed-laser excitation *Phys. Rev.* A **57** 4204–11

[51] Sukenik C I, Boshier M G, Cho D, Sandoghdar V and Hinds E A 1993 Measurement of the Casimir–Polder force *Phys. Rev. Lett.* **70** 560–3

[52] Bordag M, Mohideen U and Mostepanenko V M 2001 New developments in the Casimir effect *Phys. Rep.* **353** 1–205

[53] Sandoghdar V, Sukenik C I, Hinds E A and Haroche S 1992 Direct measurement of the van der Waals interaction between an atom and its images in a micron-sized cavity *Phys. Rev. Lett.* **68** 3432–5

[54] Hinds E A, Lai K S and Schnell M 1997 Atoms in micron-sized metallic and dielectric waveguides *Phil. Trans. R. Soc.* A **355** 2353–65

[55] Emig T, Jaffe R L, Kardar M and Scardicchio A 2006 Casimir interaction between a plate and a cylinder *Phys. Rev. Lett.* **96** 080403

[56] Laliotis A 2007 Testing the distance-dependence of the van der Waals interaction between an atom and a surface through spectroscopy in a vapor nanocell *Proc. SPIE* **6604** 660406

[57] Radnaev A G, Dudin Y O, Zhao R, Jen H H, Jenkins S D, Kuzmich A and Kennedy T A B 2010 A quantum memory with telecom-wavelength conversion *Nature Phys.* **6** 894–9

[58] Vetsch E 2010 Optical interface based on a nanofiber atom-trap *PhD Thesis* Johannes Gutenberg-Universität, Mainz

[59] Rosenbusch P, Ghezali S, Dzuba V A, Flambaum V V, Beloy K and Derevianko A 2009 ac Stark shift of the Cs microwave atomic clock transitions *Phys. Rev.* A **79** 013404

[60] Stiebeiner A, Garcia-Fernandez R and Rauschenbeutel A 2010 Design and optimization of broadband tapered optical fibers with a nanofiber waist *Opt. Express* **18** 22677–85

[61] Aoki T 2010 Fabrication of ultralow-loss tapered optical fibers and microtoroidal resonators *Japan. J. Appl. Phys.* **49** 118001

[62] Goban A, Choi K S, Alton D J, Ding D, Lacroûte C, Pototschnig M, Thiele T, Stern N P and Kimble H J 2012 in preparation

[63] Eichenfield M, Chan J, Camacho R M, Vahala K J and Painter O 2009 Optomechanical crystals *Nature* **462** 78–82

[64] Wallquist M, Hammerer K, Rabl P, Lukin M and Zoller P 2009 Hybrid quantum devices and quantum engineering *Phys. Scr.* **T137** 014001